Structures of closed and open states of a voltage-gated sodium channel

Michael J. Lenaeus[a,b], Tamer M. Gamal El-Din[a], Christopher Ing[c,d], Karthik Ramanadane[a,e,1], Régis Pomès[c,d], Ning Zheng[a,f], and William A. Catterall[a,2]

[a]Department of Pharmacology, University of Washington, Seattle, WA 98195; [b]Department of Medicine, Division of General Internal Medicine, University of Washington, Seattle, WA 98195; [c]Molecular Medicine, Hospital for Sick Children, Toronto, ON, Canada M5G 0A4; [d]Department of Biochemistry, University of Toronto, Toronto, ON, Canada M5S 1A8; [e]Department of Biology, École Normal Supérieure, 94230 Cachan, France; and [f]Howard Hughes Medical Institute, University of Washington, Seattle, WA 98195

Contributed by William A. Catterall, February 27, 2017 (sent for review January 17, 2017; reviewed by Alan L. Goldin and Guillaume Lamoureux)

Bacterial voltage-gated sodium channels (BacNavs) serve as models of their vertebrate counterparts. BacNavs contain conserved voltage-sensing and pore-forming domains, but they are homotetramers of four identical subunits, rather than pseudotetramers of four homologous domains. Here, we present structures of two $\mathrm{Na_VAb}$ mutants that capture tightly closed and open states at a resolution of 2.8–3.2 Å. Introduction of two humanizing mutations in the S6 segment ($\mathrm{Na_VAb}$/FY: T206F and V213Y) generates a persistently closed form of the activation gate in which the intracellular ends of the four S6 segments are drawn tightly together to block ion permeation completely. This construct also revealed the complete structure of the four-helix bundle that forms the C-terminal domain. In contrast, truncation of the C-terminal 40 residues in $\mathrm{Na_vAb}$/1–226 captures the activation gate in an open conformation, revealing the open state of a BacNav with intact voltage sensors. Comparing these structures illustrates the full range of motion of the activation gate, from closed with its orifice fully occluded to open with an orifice of ∼10 Å. Molecular dynamics and free-energy simulations confirm designation of $\mathrm{Na_VAb}$/1–226 as an open state that allows permeation of hydrated $\mathrm{Na^+}$, and these results also support a hydrophobic gating mechanism for control of ion permeation. These two structures allow completion of a closed–open–inactivated conformational cycle in a single voltage-gated sodium channel and give insight into the structural basis for state-dependent binding of sodium channel-blocking drugs.

sodium channels | action potential | sodium conductance | activation gate

Voltage-gated sodium ($\mathrm{Na_v}$) channels are integral membrane proteins that change conformation in response to depolarization of the membrane potential, open a transmembrane pore, and conduct sodium ions inward to initiate and propagate action potentials (1). As a result, sodium channels are paramount to nerve conduction, skeletal and cardiac muscle contraction, secretion, neurotransmission, and many other processes (2). Nevertheless, the molecular mechanisms underlying voltage-sensing and sodium conduction remain uncertain due to the size and complexity of eukaryotic $\mathrm{Na_v}$ channels, which are >200 kDa, contain 24 transmembrane segments, and remain resistant to detailed structural analysis (3).

Prokaryotic sodium channels (BacNavs), instead, have been used to study the 3D structure, mechanism of action, and pharmacology of $\mathrm{Na_v}$ channels (4). BacNavs contain the basic voltage-sensing and ion-conductance machinery of mammalian $\mathrm{Na_v}$ channels in a much smaller package—typically consisting of homotetramers of subunits with 200–300 amino acids and 6 transmembrane segments, numbered S1–S6 by convention (4–6). NaChBac (from *Bacillus haldorans*) was the first BacNav to be cloned and studied by electrophysiology (4), followed several years later by the purification, crystallization, and structure determination of its orthologs $\mathrm{Na_VAb}$ from *Arcobacter butzleri* (7, 8) and $\mathrm{Na_vRh}$ from *Ricketsialles sp.* (9), as well as pore-only constructs of $\mathrm{Na_VMs}$ from *Magnetococcus marinus* (10) and $\mathrm{Na_VAep1}$ from *Alkalilimnicola ehrlichei* (11). As predicted from structure–function studies of mammalian sodium channels, the S1–S4 segments form a voltage-sensing module in which four conserved arginine or lysine residues in the S4 segment serve as gating charges (12, 13). The S5 and S6 segments form a pore domain similar to the "inverted teepee" of prokaryotic potassium channels, and the ion selectivity filter is formed by the P loop between them (5). The activation gate is located at the intracellular end of the S6 segments (5).

The voltage sensors of $\mathrm{Na_VAb}$ and $\mathrm{Na_VRh}$ are thought to be in an activated state, based on disulfide-locking and gating pore current studies (14–17). BacNav crystal structures to date have shown a single activated conformation of the voltage sensor, but several different conformations of the pore domains, including the preopen state identified in the $\mathrm{Na_VAb}$/I217C structure and the collapsed potentially inactivated states identified in the $\mathrm{Na_VAb}$/WT and $\mathrm{Na_VRh}$ structures (5). The intracellular activation gate formed by the bundle crossing of the S6 segments has been observed in different conformations in these BacNav structures, and several models have been proposed in which conformational changes in the voltage sensor are translated into pore opening by way of a concerted, iris-like dilation of the intracellular ends of the S5 and S6 segments, mediated by twisting and bending motions of the S6 helix (5, 7, 18). However, these models remain to be validated by structural comparisons of a single BacNav channel with intact voltage-sensing domains in both closed and open states. Here, we have used $\mathrm{Na_VAb}$ constructs to study the activation gate in two additional conformations, which allow accurate modeling of

Significance

Bacterial voltage-gated sodium channels serve as models of their vertebrate counterparts because they have similar functional components in a simpler structure. We present high-resolution structures of tightly closed and open states. In the closed state, the activation gate fully occludes the conduction pathway, and the intracellular C-terminal domain is revealed as a long four-helix bundle. In the open state, the activation gate has an orifice of ∼10 Å. Molecular dynamics simulations confirm that this conformation would allow permeation of hydrated $\mathrm{Na^+}$. These structures are significant advances because they provide a complete closed–open–inactivated conformational cycle in a single voltage-gated sodium channel and give insight into the structural basis for state-dependent binding of sodium channel-blocking drugs.

Author contributions: M.J.L., T.M.G., C.I., R.P., N.Z., and W.A.C. designed research; M.J.L., T.M.G., C.I., K.R., and R.P. performed research; K.R. contributed new reagents/analytic tools; M.J.L., T.M.G., C.I., K.R., R.P., N.Z., and W.A.C. analyzed data; and M.J.L., T.M.G., C.I., K.R., R.P., N.Z., and W.A.C. wrote the paper.

Reviewers: A.L.G., University of California, Irvine; and G.L., Concordia University.

The authors declare no conflict of interest.

[1]Present address: Department of Biochemistry, University of Zürich, Winterthurerstrasse 190, 8057, Zurich, Switzerland.

[2]To whom correspondence should be addressed. Email: wcatt@uw.edu.

This article contains supporting information online at www.pnas.org/lookup/suppl/doi:10.1073/pnas.1700761114/-/DCSupplemental.

BacNav gating. Our results do not show any change in the structure of Na$_V$Ab's voltage-sensing module, but they provide two crucial snapshots of the activation gate as it transitions from closed to open states and thereby allow comparison of the S6 helix in different states of the same channel. Molecular dynamics (MD) simulations confirm that the activation gate is open and suggest a hydrophobic gating mechanism for control of ion permeation.

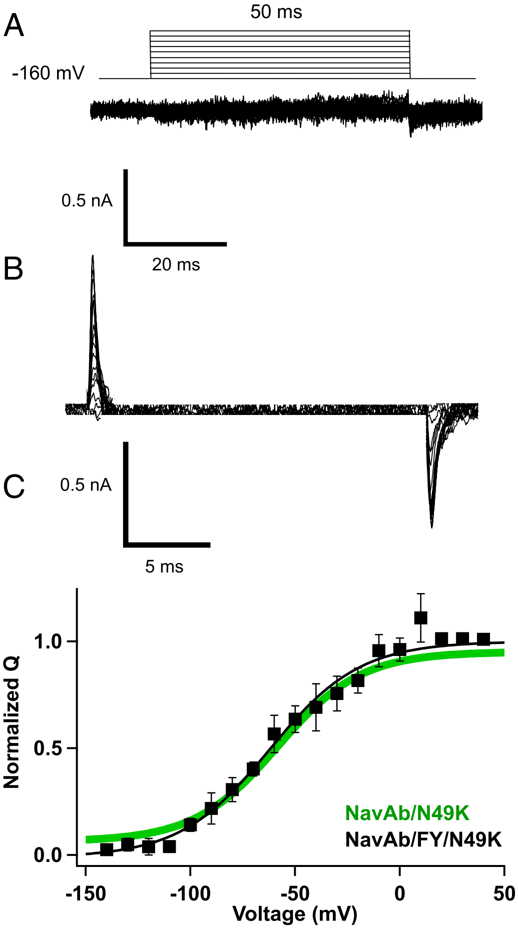

Fig. 1. Na$_V$Ab/FY conducts gating currents but not ionic currents. (*A*) No ionic currents were detected from Na$_V$Ab FY construct. (*B*) At very high expression of Na$_V$Ab FY construct, gating currents were elicited by using a voltage–clamp protocol, where depolarizing pulses were applied for 50 ms from −160 mV to +60 mV in 10-mV increments. (*C*) *Q–V* curve of Na$_V$Ab/FY. For Na$_V$Ab/FY/N49K, $V_{1/2} = -62.2 \pm 3$ ($n = 7$); for Na$_V$Ab/N49K, $V_{1/2} = -65 \pm 2.2$.

Results

Na$_V$Ab/T206F/V213Y, a Permanently Closed Na$_V$Ab Mutant. Two aromatic residues on the S6 segment in domain IV are critical for use-dependent drug binding in mammalian Na$_v$ channels: F1764 and Y1771 in Na$_V$1.2 numbering (19, 20). These residues were introduced into Na$_V$Ab by site-directed mutagenesis (Fig. S1), and the resulting mutant channel (termed Na$_V$Ab/FY) was studied by electrophysiology and X-ray crystallography. The Na$_V$Ab/FY protein was easily expressed at high levels in insect cells, but it did not show any inward sodium current under standard experimental protocols. Because of the unusually negative voltage-dependent activation of Na$_V$Ab, which might be further negatively shifted by the FY mutation, we introduced the N49K mutation to shift the voltage dependence of gating ~75 mV in the positive direction (21). High-resolution recordings of this triple-mutant construct revealed no ionic current (Fig. 1*A*), but detected gating current (Fig. 1*B*), which represents the outward movement of the gating charges in the S4 segments during the conformational change that leads to channel activation (12, 13, 22). The Q/V curve of Na$_V$Ab/FY/N49K overlapped with that of Na$_V$Ab/N49K (Fig. 1*C*), indicating that the FY mutation does not alter the voltage dependence of voltage-sensor function, even though it prevents ionic conductance. Even with extremes of voltage and high-resolution recording conditions (Fig. 1, legend), only minimal central pore current could be induced in this construct, suggesting that its pore domain was not passable by hydrated sodium ions. In light of these physiological results, this mutant provides an exceptional opportunity to examine the structure of a channel form with a permanently closed pore in the context of voltage sensors that are activated.

Na$_V$Ab/FY crystallized in an orthorhombic space group ($P2_12_12_1$) with a Na$_V$Ab tetramer as the asymmetric unit. We solved the structure using a modified Na$_V$Ab/I217C model (7) as our starting point and applying noncrystallographic symmetry (NCS) to improve electron-density maps throughout rebuilding and refinement (Table S1). Addition of the FY mutations abolished the pseudomerohedral twinning present in previous Na$_V$Ab WT structures (8), making data analysis easier and eliminating a potential source of error in structure determination. The structure of Na$_V$Ab/FY revealed a previously unrecognized conformation of the pore and activation gate and allowed visualization of the intracellular C-terminal domain (CTD) of Na$_V$Ab, as well as several additional bound detergent molecules and lipids (Fig. 2). Eight bound molecules of the detergent 3-[(3-cholamidopropyl)dimethylammonio]-2-hydroxy-1-propanesulfonate (CHAPSO) can be easily discerned in the expanded structure in Fig. 2*B* (yellow sticks), in the interface of the S4–S5 linker, the S6 activation gate, and the membrane base of the extended CTD. It is unknown whether there are endogenous lipid molecules that would occupy these positions in vivo.

The voltage sensor and selectivity filter of this double-mutant structure are similar to the previously published structure of Na$_V$Ab/I217C (rmsd for residues 11–110 in the voltage-sensing module is 0.5 Å; rmsd for residues 165–185 in the selectivity filter is 0.25 Å). However, there were significant changes in the activation gate, which we defined as S6 residues 211–221, plus the adjacent portions of the S4–S5 linker and S5 helices (Fig. 3*A*). First, the S4–S5 linker helix of Na$_V$Ab/FY was kinked outward starting at residue P128 in each segment, resulting in movement ~1 Å further away from the adjacent S6 helix for residues 128–133 (Fig. 3 *A* and *B*). These conformational changes in the S4–S5 linker with respect to S6 were small, but when combined, the net effect was to move the S4–S5 linker and base of S5 away from the S6 helix relative to their positions in the described Na$_V$Ab/I217C structure (Fig. 3*B*). Second, the S6 helix had rotated 20° around the central pore axis relative to its position in the Na$_V$Ab/I217C structure. This helical rotation resulted in tightening the S6 bundle crossing at I217 and M221, where the diameter of the channel was reduced to ~5 and ~3 Å, respectively, when calculated from the center of the atoms closest to the axis of the pore (Fig. 3*C*). Although the structure of the original Na$_V$Ab/I217C construct had a closed activation gate, with side chains of M221 completely occluding the ion conductance pathway (7), the pore of Na$_V$Ab/FY was even more tightly closed based on these distances. These results suggest that Na$_V$Ab/FY represents a deeply closed state of the pore, which must undergo stepwise conformational transitions in the activation gate to reach the preopen state of Na$_V$Ab/I217C and finally snap into the open state capable of conducting Na$^+$.

The C-Terminal Helical Bundle of Na$_V$Ab. To our surprise, the Na$_V$Ab/FY structure also showed an ordered CTD (Figs. 2*A* and 4*A*), unlike that previously described in the Na$_V$Ab/I217C and Na$_V$Ab/WT structures (7, 8). This region has been shown to influence open probability and activation kinetics in orthologs of Na$_V$Ab (11, 23), and its structure has been solved in Na$_V$Aep1 and an NaK chimera (23, 24). Na$_V$Ab's CTD formed a four-helix bundle that overlapped with the activation gate and extended from residue I217 through the C terminus of the protein at residue 266 (Fig. 4*A*). As in Na$_V$Aep1 (23),

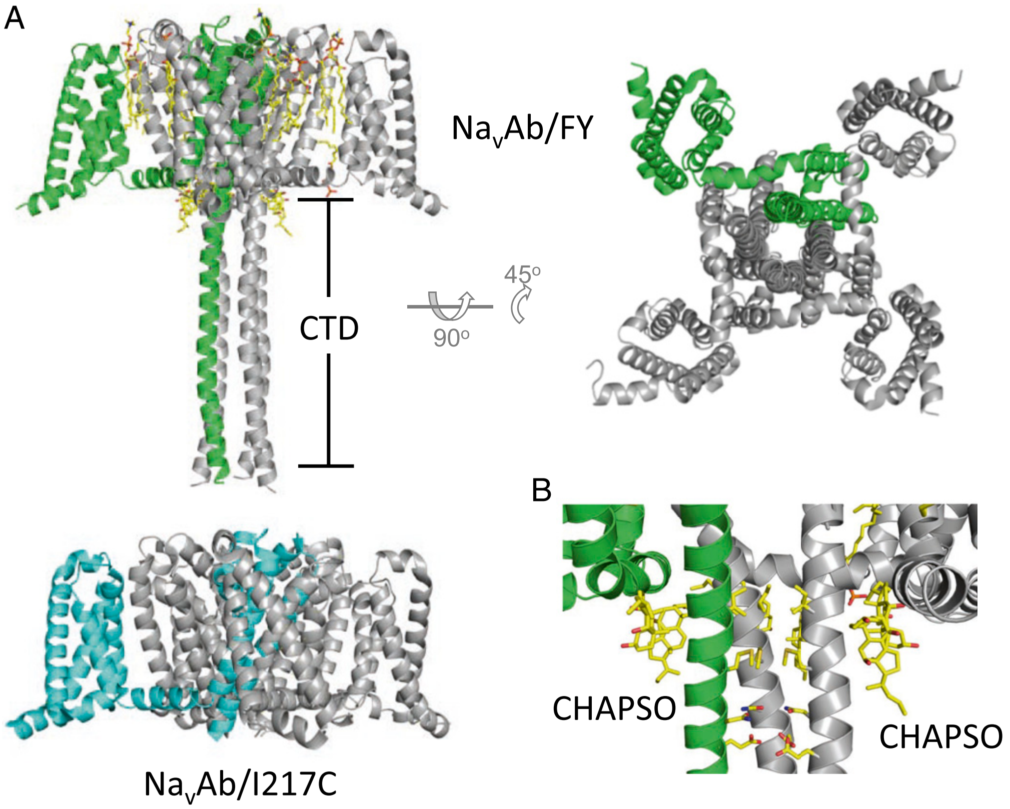

Fig. 2. The structure of Na$_V$Ab/FY. (*A*) The overall fold of Na$_V$Ab/FY and a comparison with that of Na$_V$Ab/I217C. One of four channel monomers is shown in either green or cyan to highlight the relationship between monomers. Lipid molecules are drawn in stick format. (*B*) Na$_V$Ab/FY's closed activation gate and adjacent CTD. Amino acid residues lining the activation gate and neck are shown in stick representation (I217, M221, N225, and E228), as are lipids as in *A*. One subunit of the channel and its accompanying lipids have been removed for clarity.

this domain can be split into two regions: the proximal (or "neck") portion, which contains hydrophilic residues on the interior of the four-helix bundle, and the distal portion, which is a classical four-helix bundle and contains isoleucine or leucine residues on the interior of the motif (Fig. 4 *A–C*). Arrigoni et al. (23) have proposed that the four-helix bundle in the neck of Na$_V$Aep1 unwinds and splays open to allow opening of the activation gate. Similar to Na$_V$Aep1, Na$_V$Ab's neck contained rings of hydrophilic residues (N225 and E228) on the intracellular side of the activation gate and an ion-binding site near the transition point to the coiled coil (Fig. 4 *A* and *B*). There were, however, important differences between the structure of Na$_V$Ab/FY and Na$_V$Aep1 in the proximal portion of the CTD (highlighted in Fig. 4*D*). The pi-helix motif identified in Na$_V$Aep1 was not present in Na$_V$Ab/FY, and, as such, the connection between S6 and CTD was different in secondary structure (Fig. 4*D*) and spatial orientation of the helices relative to each other (Fig. 4*E*). In contrast to Na$_V$Aep1, Na$_V$Ab contained only alpha helices in this neck region, whereas the coiled-coil motifs at the C termini of these proteins nearly overlaid each other (Fig. 4*E*). The CTD has an important influence on voltage-dependent activation and pore opening, as presented below.

Na$_V$Ab/1–226, a Mutant Captured in an Open State. Trypsin digestion of Na$_V$Ab suggested a stable transmembrane core of the protein; therefore, we made a variety of C-terminal truncations to further study gating and improve crystallization. We found that Na$_V$Ab/1–226, which lacks 40 cytosolic residues of the CTD (Fig. 5*A* and Fig. S1), can be expressed at high levels and is suitable for studies by both electrophysiology and X-ray crystallography. This construct generated a Na$_v$ current with voltage dependence and kinetics of activation and inactivation during test pulses that were similar to those for Na$_V$Ab (Fig. 5*B*). However, there was an important distinguishing feature of the truncation mutant. Na$_V$Ab/1–226 activated at more negative voltages than full-length Na$_V$Ab, suggesting stabilization of the open state relative to the closed and inactivated states (Fig. 5*C*). In contrast, there was no change in the voltage dependence of steady-state inactivation of Na$_V$Ab/1–226 (Fig. 5*D*).

These features suggested that the conformational state of Na$_V$Ab was perturbed by truncation of its CTD—a hypothesis we confirmed by X-ray crystallography. We crystallized Na$_V$Ab/1–226 containing the cysteine mutation I217C previously shown to facilitate crystallization in the full-length Na$_V$Ab channel. This mutant expressed well, could be purified easily, and could be analyzed by X-ray crystallography at high resolution (2.85 Å). Like the Na$_V$Ab/FY structure, the Na$_V$Ab/1–226 structure showed near identity to the previously described structures in the voltage sensor and ion selectivity filter (rmsd of voltage-sensing module, 0.5 Å; rmsd of selectivity filter, 0.25 Å). Its activation gate, however, was significantly changed relative to previously described Na$_V$Ab and Na$_V$Ab/FY structures (Fig. 6*A*), as highlighted by the blue arrows showing a diameter of 3.2 Å for Na$_V$Ab/FY measured from the centers of nearest-approaching carbon atoms, compared with 10.3 Å for Na$_V$Ab/1–226. These changes in the diameter of the opening of the activation gate can be seen in more detail in spacefilling representations (Fig. 6*B*). In Na$_V$Ab/FY, the side chains of I217 and M221 protrude into the lumen of the pore and fully occlude it, whereas the pore was open to the cytosol in Na$_V$Ab/1–226 (Fig. 6*B*).

The S6 helix is kinked in this structure compared with Na$_V$Ab/FY (Fig. 7, blue vs. tan). In addition, it has rotated away from the pore axis to increase the diameter of the permeation pathway to ∼10 Å at the level of residue 217, sufficient to allow permeation of a hydrated

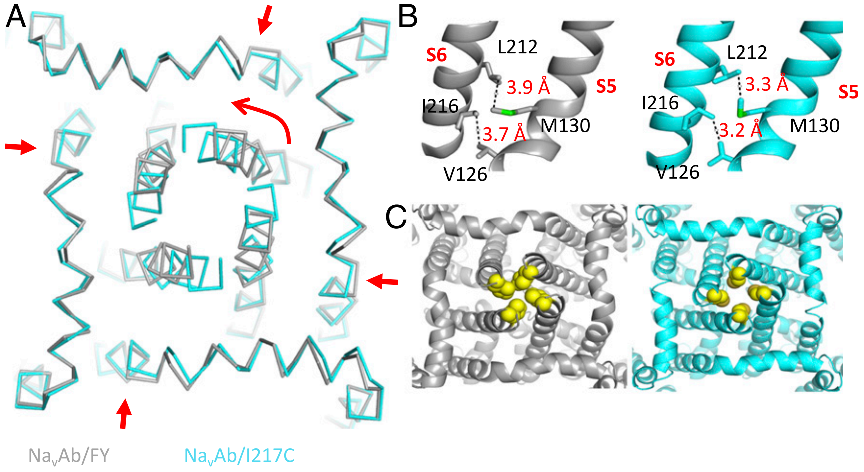

Fig. 3. Conformational changes at the activation gate. (*A*) Structures of Na$_V$Ab/FY and Na$_V$Ab/I217C are superposed in wire format. The view is as if one were below the channel and looking upward into the permeation pathway. Red arrows highlight the conformational changes described in the text—both an inward movement of the C-terminal portion of the S4–S5 linker and a rotation of the distal portion of the S6. (*B*) Close-up view of the interface between the S4–S5 linker and the S6 helix at the level of the activation gate. Na$_V$Ab/FY is on the left in gray, and NavAb/I217C is on the right in cyan. Helices are show in cartoon format; side chains as sticks; and atom distances are shown in red. (*C*) The view of the closed activation gate in Na$_V$Ab/FY (*Left*; gray) and Na$_V$Ab/I217C (*Right*; cyan), with orientation as in *A*. Helices are shown in cartoon format, and side chains of I217 (for Na$_V$Ab/FY) and C217 (for Na$_V$Ab/I217C) are shown as yellow spheres.

sodium ion (see below). The kink at T206 corresponds to the hinge residue identified in structure–function experiments on prokaryotic sodium and potassium channels (25–28). On the intracellular end of S6, the conformation has clearly changed from the Na$_V$Ab/FY structure to the Na$_V$Ab/1–226 at the level of positions 217 and 221, resulting in a more open permeation pathway compared with all other Na$_V$Ab structures (Fig. 7).

To illustrate the preferential movement of the activation gate in the Na$_V$Ab/1–226 structure, we plotted the pore diameters measured at the Cα positions of the residues in the full S6 helix from extracellular vestibule (V) to intracellular activation gate (Fig. 8*A*). The pore diameters in Na$_V$Ab/FY (closed), Na$_V$Ab/1–226 (open), and Na$_V$Ab/WT (inactivated) are similar from the extracellular vestibule to the central cavity (CC), but differ strikingly at the activation gate which is closed in Na$_V$Ab/FY, wide open in Na$_V$Ab/1–226, and intermediate in Na$_V$Ab in the inactivated state. The changes in diameter of the activation gate at position 217, as observed from the intracellular side of the membrane, are illustrated in spacefilling format in Fig. 8*C*. These images confirm that Na$_V$Ab/FY is tightly closed, Na$_V$Ab/1–226 is open, and the slow-inactivated state observed for Na$_V$Ab/WT (8) is intermediate and asymmetric in shape.

The CC (Fig. 8*A*), located in the lumen of the pore on the extracellular side of the activation gate, is a target site for binding of sodium channel-blocking drugs used in local anesthesia, cardiac arrhythmia, and epilepsy (7). Even though the Cα positions are not altered very much in transitions among these states, the twisting/bending motion of the S6 segment changes the positions of side chains Na$_V$Ab/1–226 compared with Na$_V$Ab/FY, as illustrated for T206 in Fig. 8*B*. The change in the conformation of this drug-receptor site indicates that transition from the open state to the deep resting state represented by Na$_V$Ab/FY is likely to have substantial effects on drug binding. A well-known feature of drug block of sodium channels is hyperpolarization-dependent drug dissociation, in which prolonged hyperpolarization reverses pre-established drug block (29, 30). This rearrangement of the amino acid side chains involved in drug binding in the deep closed state represented by Na$_V$Ab/FY may contribute to this important aspect of state-dependent drug block and unblock.

Structural Fluctuations, Hydration, and Cation Permeation in the Open State of Na$_V$Ab/1–226. To examine the interplay of hydration, ion permeation, and structural fluctuations of the activation gate, we performed multiple MD simulations of Na$_V$Ab/I217C and Na$_V$Ab/1–226 in a hydrated lipid bilayer in the microsecond time range (*Methods*). Because the Na$_V$Ab/1–226 structure is a static snapshot of an apparently open conformation of the activation gate, we first examined results obtained by using harmonic restraints to keep the S6 helices close to the crystallographic structure of the open state. In these simulations, we observed a distribution of pore diameters at the centers of the S6 helices at the activation gate (Fig. 9*A*, blue), with a mean of 17.4 ± 0.1 Å. In this restrained open state, there were relatively small fluctuations in the asymmetry of the S6 helices, as illustrated by the small deviations from the diagonal line in Fig. 9*D*. The mean hydration of the activation gate in this open-state structure was 15.1 ± 0.8 water molecules (Fig. 10*A*, blue). Na$^+$ moved through this bottleneck with an average of 5.3 ± 0.1 water molecules in its inner hydration shell, compared with 5.8 ± 0.1 in free solution, indicating that passage through the open activation gate requires only the loss of ∼0.5 water molecule in the inner hydration shell of Na$^+$ (Fig. 10*D*). The estimated free energy barrier for Na$^+$ permeation was ∼2 kcal/mol (Fig. 10*F*), comparable with the free energy barrier for movement of Na$^+$ through the selectivity filter (31). Together, these results are consistent with the conclusion that the Na$_V$Ab/1–226 structure captured by X-ray crystallography has an open activation gate, which presents no significant barrier to Na$^+$ permeation.

To study the effect of thermal fluctuations of the activation gate, we conducted similar simulations without restraints. In unrestrained simulations initiated in the Na$_V$Ab/1–226 or the Na$_V$Ab/I217C conformation, the activation gate spontaneously underwent moderate contraction and dilation, with changes in the average diagonal distances from the centers of the cylinders of the S6 α helices from 18.2→15.7 ± 0.2 Å and 13.9→15.0 ± 0.1 Å, respectively (Fig. 9*A*, black and red). Thermal fluctuations often led to significant deviations from the symmetric arrangement of the S6 helices, as shown by the deviations from the diagonal line in Fig. 9*B* (black and red). The activation gate bottleneck was completely dehydrated (dewetted) in the Na$_V$Ab/I217C preopen state (Fig. 10 *A*–*C*, black), whereas it fluctuated between 0 and 25 water molecules, with an average of 7.3 ± 0.4, in unrestrained Na$_V$Ab/1–226 (Fig. 10 *A*–*C*, blue).

To examine the effect of the hydrophobic side chains on the structure and properties of the activation gate, we replaced both C217 and V213 by alanine (Na$_V$Ab/AA) and repeated the simulations successively with and without restraints on helix position. In the restrained simulations, this double mutation resulted in a shift of helix geometry toward the open state relative to WT (17.5 ± 0.1 vs. 15.7 ± 0.2 Å; Fig. 9 *A*, *D*, and *E*) and greater hydration (Fig. 10 *A*–*C*). Because of the smaller side chains, average pore hydration in Na$_V$Ab/AA was greater than in Na$_V$Ab/I217C in both unrestrained and restrained simulations (20.5 ± 0.6 and 21.3 ± 0.2 water molecules, respectively). As such, Na$^+$ hydration in the activation gate only dropped to 5.5 ± 0.1 in the double mutant (Fig. 10*D*). However, this additional hydration had no effect on the free energy barrier for Na$^+$

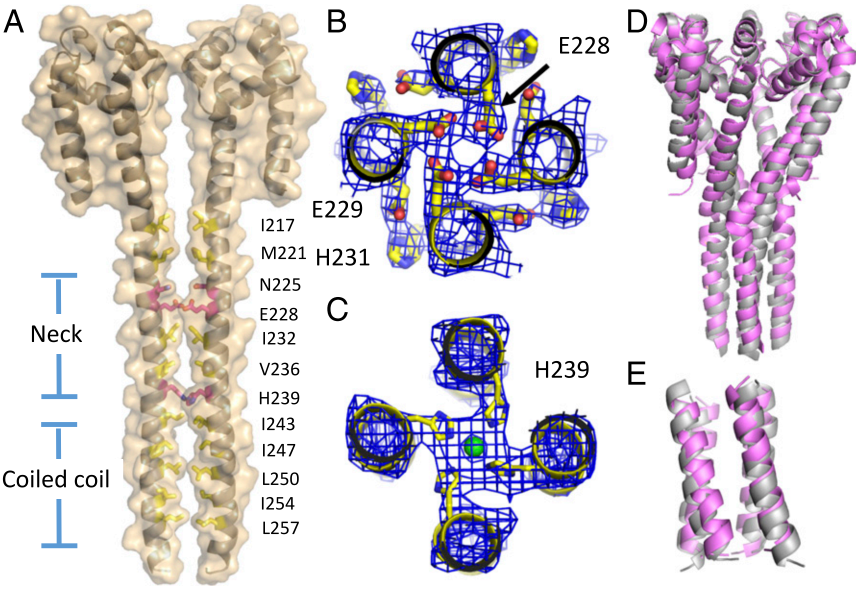

Fig. 4. The CTD of Na$_V$Ab/FY. (*A*) Two of four Na$_V$Ab/FY monomers are shown as transparent surfaces, with underlying cartoons. Residues lining the CTD have been drawn in stick format, with hydrophilic residues highlighted in magenta and hydrophobic residues highlighted in orange. (*B*) Exemplar electron density of Na$_V$Ab/FY CTD neck, showing a ring of E228 hydrogen-bound to itself and an intersubunit hydrogen bond between E229 and H231. Helices are drawn in cartoon style, with side chains highlighted as sticks. Electron density is 2Fo–Fc calculated at 1.5 σ. (*C*) Exemplar electron density of Na$_V$Ab/FY CTD coiled-coil at the level of H239, highlighting the hydrophobic nature of the four-helix bundle at this level. Helices and side chains are displayed as described above. Electron density is 2Fo–Fc calculated at 1.5 σ, and chloride ion is shown as a green sphere. (*D*) Superposition of Na$_V$Ab/FY pore and neck (gray) and Na$_V$Aep1 pore and neck (light pink; PDB ID code 5hk7), with the voltage sensors and S4/S5 linkers of Na$_V$Ab/FY removed for clarity. (*E*) Superposition of Na$_V$Ab/FY coiled-coil (gray) with that of NavAep1.

movement, which was indistinguishable from that obtained from restrained simulations of the open Na$_V$Ab/I217C channel (Fig. 10*F*).

Together, the MD simulation results confirmed that the crystallographic structure of Na$_V$Ab/1–226 corresponds to an open state of the Na$_V$Ab pore, for which the activation gate induces a small desolvation penalty of ∼2 kcal/mol relative to the aqueous state. Structural relaxation led to a partial collapse and partial dehydration of the activation gate, which resulted in doubling the height of the Na^+ desolvation barrier to 4 kcal/mol, and to asymmetric fluctuations of the activation gate that were also observed in the closed state of the channel. These effects all but disappeared in the Na$_V$Ab/AA double mutant of the S6 helix, which remained close to the crystallographic structure of the open state, even in the absence of helix restraints. These results support a hydrophobic-collapse model for closure of the activation gate.

Discussion

S6 Mutations Reveal the Structure of Na$_V$Ab's Intracellular CTD. Our FY structure revealed the conformation of the CTD of Na$_V$Ab in a closed state of the pore. It is a four-helix bundle similar to that observed in other BacNav channels and prokaryotic K^+ channels, as well as the pore-only construct of Na$_V$Aep1 and a NaK chimera (23, 24). In the highest-resolution structure of Na$_V$Aep1 (2.95 Å), the portion of the CTD nearest to the pore contained a pi-helix that accommodated a centrally oriented tryptophan residue coordinating a chloride ion in the middle of the four-helix bundle. The Na$_V$Ab structure lacks this feature. Instead, there is a continuous alpha helix with two centrally oriented rings of polar residues (N225 and E228) in an equivalent position. This structure of the C terminus of Na$_V$Ab may contribute to its voltage dependence of activation, because removing the C terminus in Na$_V$Ab/1–226 favored channel activation and pore-opening.

Closed States of the Pore. The FY mutation rendered the pore of Na$_V$Ab/FY constitutively closed at the intracellular activation gate, even though three gating charges in the voltage sensors were in their outward, activated positions. Upon depolarization from the very negative membrane potential characteristic of the resting state of Na$_V$Ab (less than −180 mV) (7, 8), the S4 segments in the voltage-sensing modules are thought to move outward in response to the change in electrical field to reach an activated state, but the FY mutation has trapped the pore in a tightly closed conformation characteristic of the deeper resting states of Na$_V$Ab. The mutation in Na$_V$Ab/FY may prevent the kink and rotation of the S6 segment that opens the pore, and thereby uncouple the conformational change of the voltage sensor from opening the activation gate because of the high energy needed to rewet and open the dehydrated, closed activation gate. It is also conceivable that the Na$_V$Ab/FY structure represents an artifactual state of the activation gate imparted by the introduction of bulky hydrophobic residues in S6, but we consider this possibility to be unlikely because the mutations made are characteristic of mammalian Na$_V$ channels, and the voltage sensor continues

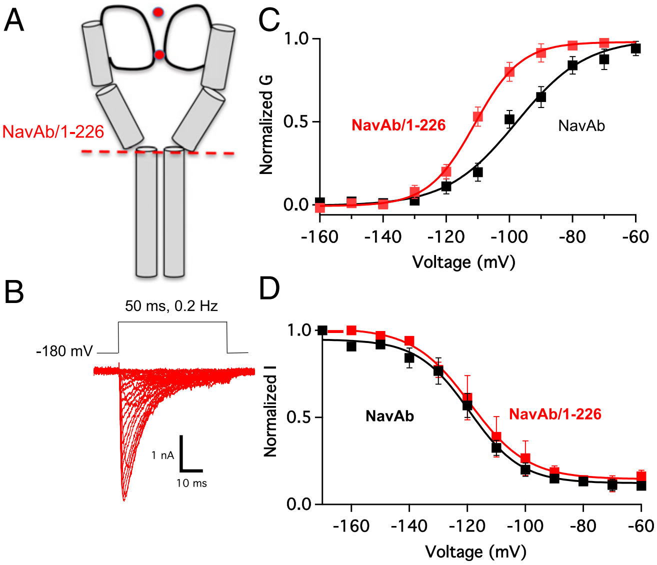

Fig. 5. Negatively shifted voltage dependence of activation for Na$_V$Ab/1–226. (*A*) Cartoon of Na$_V$Ab/1–226 pore domain and C terminal. (*B*) Current traces in response to 50-ms depolarizations from a holding potential of −180 mV in 10-mV increments. (*C*) *G–V* curves of Na$_V$Ab WT ($V_{1/2} = -97.8 \pm 1.3$ mV, $K = 11 \pm 1.2$) and Na$_V$Ab/1–226. ($V_{1/2} = -110.7 \pm 1.2$ mV, $k = 7.3 \pm 0.3$). *G–V* curves were constructed from peak current measurements of *I–V* curves (n = 5–10; *Methods*). (*D*) Steady-state inactivation curves of Na$_V$Ab WT ($V_{1/2} = -119.3 \pm 0.8$ mV, $K = 8.9 \pm 0.7$) and Na$_V$Ab/1–226 ($V_{1/2} = -116 \pm 4.4$ mV, $k = 9.8 \pm 0.7$; n = 3–6). Inactivation currents were obtained by applying a 100-ms conditioning prepulse to membrane potentials ranging from a holding potential −180 to 0 mV in 10-mV increments and were measured by using a 10-ms pulse to −10 mV at each step.

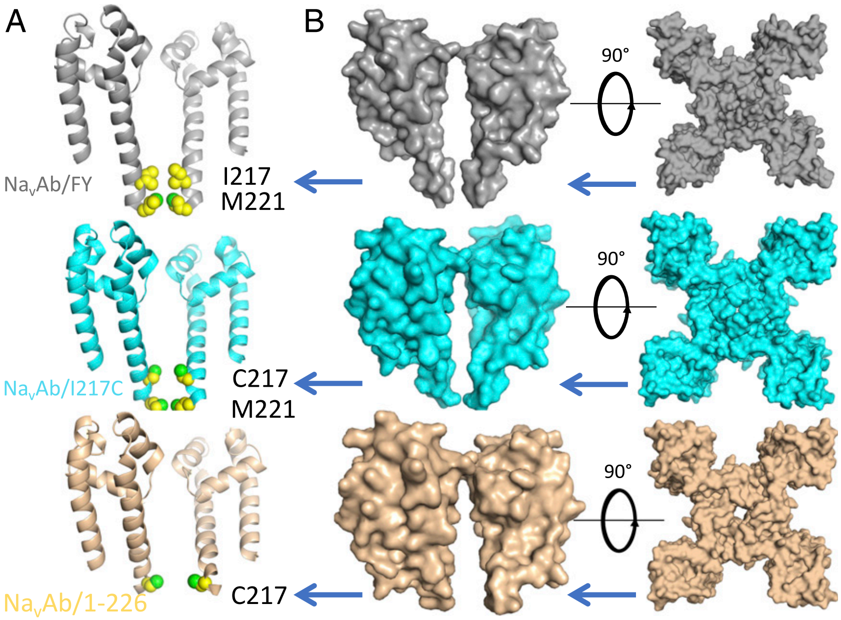

Fig. 6. Comparison of the activation gates of Na$_V$Ab/FY, Na$_V$Ab/I217C, and Na$_V$Ab/1–226. (*A*) The activation gates of Na$_V$Ab/FY (gray), Na$_V$Ab/I217C (cyan), and Na$_V$Ab/1–226 (wheat) are indicated with blue arrows. Proteins are in ribbon representation, with two of four monomers and voltage sensors removed for clarity, and space filling representation of activation gate residues I217, M221 (above), and C217 (below). (*B*) Surface representation of Na$_V$Ab/FY (gray), Na$_V$Ab/I217C (cyan), and Na$_V$Ab/1–226 (tan), showing the difference in diameter across the activation gate (blue arrow). The activation gate measures 3.2 Å across at M221 in the Na$_V$Ab/FY structure and 10.3 Å across at C217 in the Na$_V$Ab/1–226 structure at the centers of the nearest C atoms.

to function normally. Moreover, the structure of Na$_V$Ab/1–238 has a similar deeply closed activation gate with no mutation in the S6 segment (32). Mammalian sodium channels may have a larger CC that accommodates the movements of the FY residues without uncoupling from the normal voltage-sensing and gating cycle. Further support for the significance of the structure of Na$_V$Ab/FY comes from comparison with MD simulations of K$_V$ channels. In long simulations of K$_V$ gating, large hyperpolarizations caused the pore to collapse and dehydrate, expelling water from the CC (33). The resulting K$_V$ channel structure resembles the Na$_V$Ab/FY structure in this respect, because the cavity of Na$_V$Ab/FY would contain far fewer water molecules than that of Na$_V$Ab/I217C or Na$_V$Ab/1–226.

Na$_V$Ab/FY has three characteristics expected of a closed state. First, the bundle crossing is tightly closed, with narrowing at I217 and M221, making the orifice small enough to occlude hydrated Na$^+$. Second, the S6 helix maintained its helical conformation throughout its entirety (Fig. 3*C*), a feature known to favor the closed state based on previous electrophysiological data in NaChBac and analysis of the open form of the pore-only Na$_V$Ms construct (27, 34). Third, the S6 bundle crossing and selectivity filter have not adopted the asymmetric conformation previously observed in the inactivated state structures of Na$_V$Ab and Na$_V$Rh (8, 9). We believe this structure represents a previously unrecognized view of a "fully closed" activation gate in a BacNav channel and provides a starting point for more refined models of pore opening in these channels and their eukaryotic homologs.

The Na$_V$Ab/FY structure further demonstrates the structural plasticity of the S4–S5 linker region, as previously suggested by comparison of the inactivated-state structure of Na$_V$Ab/WT compared with that of Na$_V$Ab/I217C (8). The C-terminal region of the S4–S5 linker, in particular, has been found in multiple conformations in BacNav structures, suggesting a key role for residues 128–133 in gating of Na$_V$Ab. This region has also been found in different conformations in TPC structures (35, 36). Comparison of mammalian sequences shows a general pattern of flexible amino acids with a conserved hydrophobic "finger" (either L or I) at the position corresponding to Na$_V$Ab M130. Our data suggest that this position tunes channel opening by functioning as both a hydrophobic barrier to excess opening of the channel's permeation pathway, as well as a pinch point that can bend the S6 below the level of the activation gate.

Open State of the Pore. Our C-terminal truncation of Na$_V$Ab favors the transition to the open state in situ. We believe that our structure of the Na$_V$Ab/1–226 indeed represents an open state of Na$_V$Ab for three reasons. First, the S6 helix has adopted the kinked conformation suggested in prior structure–function studies of NaChBac (26, 27, 37) and the pore-only open-state structure of Na$_V$Ms (10) (Fig. 3 *B* and *C*). Second, crystallographic B factors are increased in this region of the protein relative to surrounding residues, suggesting an increase in flexibility and thermal motion (Fig. S2). Third, the width across the bundle crossing, measured from the centers of the nearest atoms, has increased approximately twofold at the level of residue 217, to a distance that would accommodate the passage of hydrated Na$^+$ according to our MD simulations. Flexibility by way of kinking and bending motions are common features of membrane proteins and transporters, and represent relatively low-energy ways to impart structural change in a membrane environment (38). They are also seen in a number of

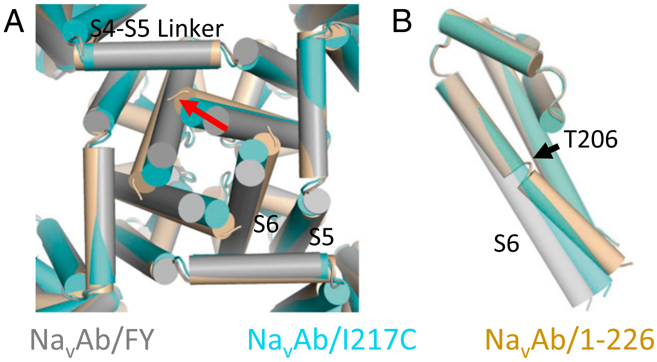

Fig. 7. Comparison of Na$_V$Ab/FY, Na$_V$Ab/I217C, and Na$_V$Ab/1–226. (*A*) Cartoon representation of the three structures of Na$_V$Ab shows the change in the position of S6 from as closed (Na$_V$Ab/FY), to preopen (Na$_V$Ab/I217C), to open (Na$_V$Ab/1–226) states. The view is from below the channel. A red arrow is shown to represent the movement of the S6 helix as the channel moves through these states. (*B*) Side view of one pore module of each construct.

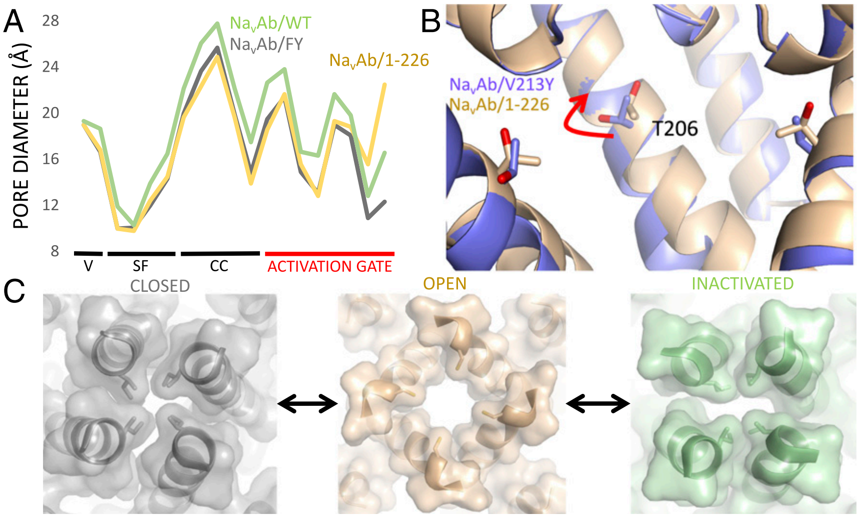

Fig. 8. Comparing the diameter of the permeation pathway in closed, preopen, and open states of the pore. (*A*) The pore diameter as measured by Cα position (*y* axis) is shown as a function of position along the permeation pathway, including the external vestibule (V; residues 180–181), selectivity filter (SF) (residues 176–178), the CC-lining residues (CC; residues 206–210), and activation gate (residues 211–218) as discussed in the text. Na$_v$Ab/FY is shown in gray, Na$_v$Ab/1–226 is shown in wheat, and Na$_v$Ab/WT is shown in green. (*B*) Close-up view of the CC of Na$_v$Ab, highlighting the side chain of T206 and its conformational change as Na$_v$Ab enters the preopen state. Na$_v$Ab V213Y, a single mutant with similar properties to those of Na$_v$Ab/FY, is shown in purple, and Na$_v$Ab/I217C is shown in cyan. The Na$_v$Ab V213Y structure was solved to 3-Å resolution under nearly identical conditions and shows the same closed, activation gate conformation observed in Na$_v$Ab/FY, though it was excluded from broad analysis here due to relatively poor electron density throughout the CTD. We use Na$_v$Ab V213Y here to allow direct comparison of the position of T206 between closed and preopen states—such an analysis is impossible with our FY construct due to the phenylalanine mutation at position 206. (*C*) Close-up view of the activation gate at the level of residue 217. The view is as if one were below the channel and looking upward upon the permeation pathway. Na$_v$Ab/FY is shown in gray, Na$_v$Ab/1–226 is shown in wheat, and Na$_v$Ab/WT is shown in green—with each model containing cartoon helices, transparent surface representation, and stick representation of the side chain at position 217.

related proteins including prokaryotic K$^+$ channels, where an analogous position serves as both a gating hinge and a modulator of inactivation (25, 28, 39).

In the structure of Na$_V$Ab/1–226, additional outward movement of the S6 segments away from the central axis would be prevented by the S4–S5 linkers from each subunit, which form a square corral to prevent further opening. The bulky side chain of M130 causes steric hindrance with that of I216 and prevents further movement, and the side chain of M130 has taken the position that would normally be taken by that of I216 if S6 were to remain an ideal alpha-helix. In this region, the conformation of Na$_V$Ab with intact voltage sensors differs from the open state structure of Na$_V$Ms with voltage sensors deleted because in Na$_V$Ms there is no S4–S5 linker helix. Lacking the constraint of the S4–S5 linker, the residue that is equivalent to I216 in Na$_V$Ms lies in a position that would clash with the S4–S5 linker, whereas I216 is rotated away from this position by way of the helix kink in Na$_V$Ab/1–226. Because of the constraints imposed by the S4–S5 linker, we believe that the structure of Na$_V$Ab/1–226 represents the most open conformation possible for the S6 activation gate in Na$_V$Ab.

Gating of Cation Permeation by Hydrophobic Collapse. The interplay of pore dilation, hydration, and free energy for ion permeation observed in our MD simulations is consistent with the notion of a hydrophobic activation gate, as previously proposed for other ion channels, including K$_V$ channels (40–43). In a hydrophobic gate, changes in the size of a narrow hydrophobic segment of the lumen shift the equilibrium between hydrated (wetted) and dehydrated (dewetted) states, enabling or precluding the passage of ions. As such, sharp wetting/dewetting transitions that are coupled to changes in the relative arrangement of pore helices mediate opening and closing of the activation gate. Consistent with such a hydrophobic gating mechanism, in our MD simulations of the Na$_V$Ab/I217C and Na$_V$Ab/1–226 channels, the closed conformation is characterized by a persistent dewetted state, whereas in the open state, the water count in the activation gate undergoes fluctuations between wetted and dewetted states. Furthermore, not only does the Na$_V$Ab/AA mutation free up space in the hydrophobic bottleneck by reducing the length of side chains, but also the pore helix bundle is more dilated than in Na$_V$Ab/1–226, indicating coupling between hydrophobic collapse of the side chains in the activation gate and pore helix contraction. When the hydrophobic cavity is small because of larger hydrophobic side chains, the pocket is dewetted and collapses, whereas when the cavity is larger because of smaller hydrophobic side chains, the activation gate is hydrated and expands. Thus, pore dilation and hydration reinforce each other. In Na$_V$Ab/AA, the cavity is large enough to displace the equilibrium toward the wetted state, and the S6 helices relax to a more open arrangement. The fact that the additional hydration in Na$_V$Ab/AA does not change the small desolvation penalty for movement of Na$^+$ confirms that the crystallographic structure of Na$_V$Ab/1–226 corresponds to the fully open state of the activation gate.

Implications for State-Dependent Drug Binding. Local anesthetic and antiarrhythmic drugs are thought to bind to a receptor site in the CC of the pore (1). Frequent opening of the pore enhances drug binding and block. Our structure of Na$_V$Ab/1–226 reveals how these drugs gain access to their receptor site, because the diameter of the open activation gate (10 Å) is large enough to allow passage of typical local anesthetic and antiarrhythmic drug molecules. Bound local anesthetic and antiarrhythmic drugs are expelled from their receptor site by strong hyperpolarization (29, 30). Our structure of Na$_V$Ab/FY illustrates a possible mechanism for this canonical feature of drug block. In the state captured in this structure, the S6 segments lining the CC have changed conformation in the closed and open states we have characterized here, and the side chains of key amino acid residues have moved significantly. Therefore, voltage-dependent unblocking of Na$_V$ channels may result from hyperpolarization-dependent transition to a deep resting state similar to Na$_V$Ab/FY and the deep resting states observed in MD simulations of K$_V$ channels (33), which have an altered conformation of the drug binding site in the CC.

Refining the Closed–Open–Inactivated Model for Na$_v$Ab. Models of pore domain movement have been incomplete because of the absence of a closed activation gate structure in a full-length channel and the absence of a voltage sensor in the pore-only models of the open state (18, 35, 36). Models of activation gating in Na$_V$ channels were heavily influenced by the putative hinge glycine in prokaryotic K$^+$ channels (25), which plays a key role in the activation of NaChBac (27, 44). However, other BacNav orthologs do not have a glycine in the equivalent position and lack an obvious hinge residue in the S6 segment. The structure of

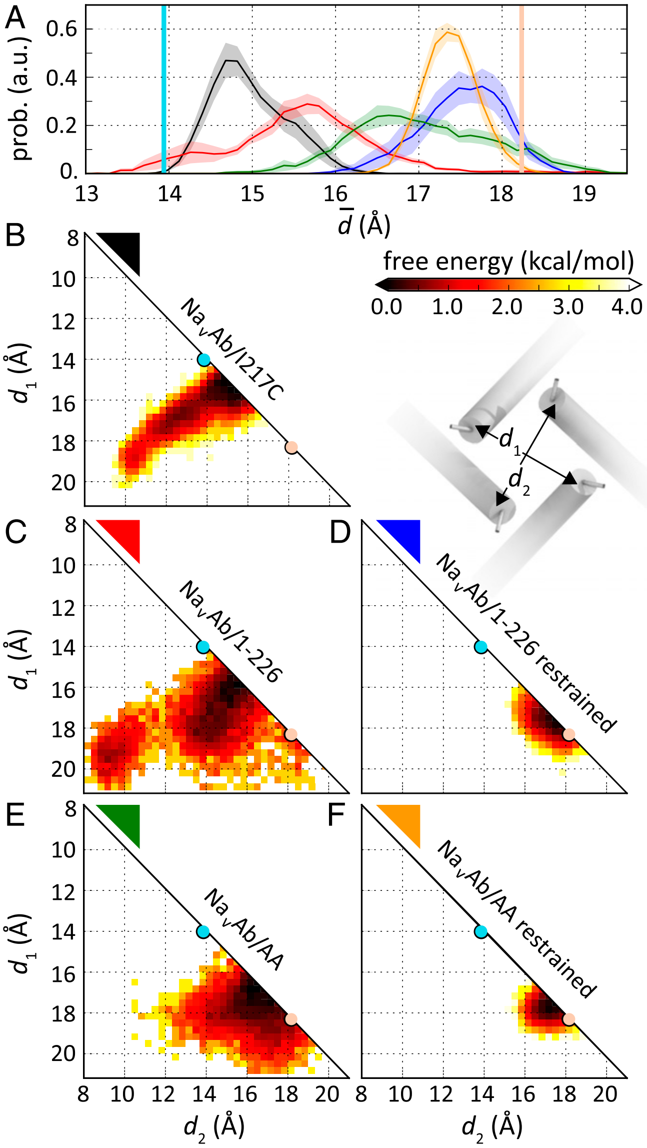

Fig. 9. Structural fluctuations of the activation gate. (*A*) Probability distribution of the mean diameters of the activation gate. Na$_V$Ab/I217C, black; Na$_V$Ab/1–226 restrained open, blue; Na$_V$Ab/1–226, unrestrained, red; Na$_V$Ab/AA restrained open, tan; Na$_V$Ab/AA unrestrained. a.u., arbitrary units; prob., probablility. (*B*) Free energy of the pairwise distances of residue 215–218 Cα atom center of mass in diagonal subunits, d_1 and d_2, from molecular simulations with several channel models. (*B*–*F*) Free energy profiles are shown for: top row, Na$_V$Ab/I217C preopen state without TM restraints (black; *B*); middle row, Na$_V$Ab/1–226 without (red; *C*) and with (blue; *D*) TM restraints; and bottom row, Na$_V$Ab/V213A/C217A (Na$_V$Ab/AA) without (*E*) and with (*F*) TM restraints. The average pairwise distance of diagonal subunits in the open- and closed-state crystal structures are shown as pink and blue circles, respectively. *Inset*, a schematic representation of distances d_1 and d_2.

Na$_v$Ab/I217C suggested a key state-dependent interaction of the voltage sensor with the base of S5 and subsequent iris-like dilation of the activation gate caused by subtle bending and twisting motions distributed along the S6 segment (7). A pore-only model of the open state suggested that activation gating occurs with a local bending motion in S6 (18), similar to that suggested in the original glycine hinge models (25–27). Our data refine these models by identifying two previously unrecognized conformations of Na$_V$Ab's S6 helix—a straight form present when the pore is tightly closed and a kinked form that develops during pore opening, probably in concert with movement in the voltage sensor, the S4–S5 linker, and the S5 segment.

In this revised model, gating begins with movement in the S4 segment, which is then coupled to movement in the S4–S5 linker, and propagated to S5 and S6 through internal protein interactions. These motions of the S5 and S6 segments have direct effects at the activation gate and indirect effects that allow the S6 segment to adopt the kinked conformation visualized in the Na$_V$Ms and Na$_V$Ab/1–226 structures. Our truncated Na$_V$Ab/1–226 construct has allowed visualization of the kinked form due to removal of its natural constraint, the CTD. The twisting/bending motion of the rigid helical form of S6 may be driven in part by exchange of hydrogen bonds of T206 from the nearby pore helix to the S6 helix itself.

Comparison with Gating of Eukaryotic Na$_V$ Channels. Studies of cysteine accessibility suggested that the activation gate in Na$_V$1.4 is located at the position of I217 in Na$_V$Ab (45, 46). These data are in good agreement with our structures and suggest that the activation gate in BacNavs is similar to that in Na$_V$1.4 domain IV, consisting of a hydrophobic barrier at the position of I217. M221 provides another hydrophobic barrier to permeation in Na$_V$Ab and some other BacNav structures. The analogous residue does not prevent access of cysteine probes to S6 residues in domain IV in the resting state of Na$_V$1.4, but the residues present at equivalent locations in other domains of eukaryotic Na$_V$ channels may restrict passage through the activation gate.

Our data also inform modeling of activation gating in vertebrate Na$_V$ channels, particularly with regard to conformational changes in the S6 segment. The residue homologous to T206 is coupled to movements of the domain III voltage sensor, as assessed by voltage–clamp fluorometry studies of Na$_V$1.5 (47, 48). It has also been hypothesized as a gating hinge for opening movements of D1–D3 in Na$_V$ channels (27). Sequence alignment of human isoforms of Na$_V$ channels shows that this residue and its neighbor are highly flexible in D1–D3, with each one containing a glycine and a small polar amino acid, either serine or asparagine. Such combinations are likely to produce helical breaks or kinks similar to the one we have identified in Na$_V$Ab/1–226, and this process may explain the differential kinetics between opening of D1–D3 and D4, which has the less flexible amino acids SF in this location (49). Our results support the hypothesis that D1, D2, and D3 pore domains open more easily due to conformational flexibility in the S6 segment, whereas D4 opens more slowly due to the more rigid S6 conformation noted. This portion of the channel also plays a key, rate-limiting role in fast inactivation (50).

Methods

Electrophysiology. *Trichopulsia ni* insect cells (Hi5 Cells) were grown on 35-mm Petri dishes. They were incubated in Grace's insect medium (Gibco) supplemented with FBS (10%) and antibiotics (100 μg/mL streptomycin and 100 U/mL penicillin). Cells were infected by replacing the incubation medium with a medium containing the virus encoding NavAb constructs (10 μg/mL). After 1 h, 2 mL of incubation medium was added to the virus-containing medium. Cells were maintained at 25–27 °C for at least 24 h before study (21). All constructs showed high-level expression that enabled us to measure ionic current and gating currents 24–48 h after infection. For gating current measurements, incubating cells for 48 h (after infection) was necessary for detecting currents. Whole-cell sodium currents were recorded by using an amplifier (Axopatch 200; Molecular Devices) with glass micropipettes (2–4 MΩ). Capacitance was subtracted and series resistance was compensated by using internal amplifier circuitry; 85–90% of series resistance was compensated. For ionic current measurements, the intracellular pipette solution contained (in mM): 35 NaCl, 105 CsF, 10 EGTA, and 10 Hepes, pH 7.4 (adjusted with CsOH). The extracellular solution contained (in mM): 140 NaCl, 2 $CaCl_2$, 2 $MgCl_2$, and 10 Hepes, pH 7.4 (adjusted with NaOH). For gating current measurements, the intracellular pipette solution contained (in mM): 140 *N*-methyl-D-glucamine (NMDG)–F, 5 mM choline–Cl, 10 mM Hepes–NMDG, and 10 mM EGTA–NMDG, pH 7.4 (adjusted with H_2SO_4). The extracellular solution contained (in mM): 140 NMDG–$MeSO_3$, 2 $CaCl_2$, and 10 Hepes–NMDG, pH 7.4 (adjusted with H_2SO_4). For constructs made on the background of WT, the standard clamp protocol for measuring ionic currents consisted of steps from a holding potential of −180 mV to voltages ranging from −180 to +50 mV in 10-mV steps. For mutants made on N49K background, the holding potential

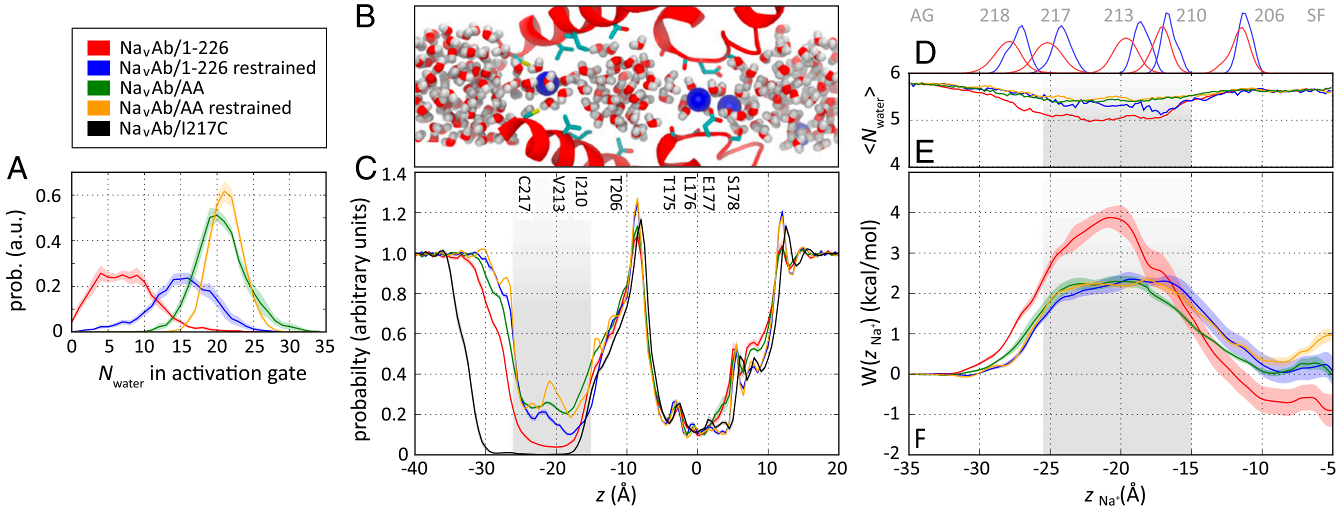

Fig. 10. Hydration and free energy of Na^+ conduction through the activation gate. (*A*) Distribution of the number of water molecules, N_{water}, in the activation gate. Color coding is indicated in the key. (*B*) Snapshot of the unconstrained Na_VAb/1–226 I217C channel with one Na^+ cation in the activation gate and two Na^+ cations in the selectivity filter shown as blue spheres. Two pore domain monomers are shown as red ribbons with selected side chains indicated below. Water molecules are shown as red and white licorice. (*C*) Distribution of water molecules along the pore axis. Scale and alignment are identical to *B*. The activation gate is highlighted in gray shading. (*D*) Axial distribution of Cα atoms of selected side chains lining the activation gate and the CC of the channel from restrained (blue) and unrestrained (red) simulations of Na_VAb/1–226 I217C. AG, activation gate; SF, selectivity filter. (*E*) Average number of water molecules in the first hydration shell of Na^+ from bulk water (left) to the CC (right). (*F*) PMF profiles $W(z_{Na^+})$ for movement of a Na^+ ion along the pore axis. Differences in the free energy of Na^+ in the CC ($z > -15$ Å) are due to fluctuations in the number of cations present in the selectivity filter. In *C*, *E*, and *F*, the 11-Å-wide barrier region is highlighted in gray shading. Data for Na_VAb/I217C are only shown in *C* because the long, narrow dehydrated intracellular activation gate precludes the passage of Na^+ ions.

was −140 mV, and pulses were applied from −140 to +50 mV in 10-mV steps. Gating currents were measured from holding potential −160 mV. Cells were held at −160 mV for 2 min, and short 20-ms pulses were applied from −160 up to +40 mV in 10-mV steps. Voltage–clamp pulses were generated and currents were recorded by using Pulse software controlling an Instrutech ITC18 interface (HEKA). Data were analyzed by using Igor Pro-6.2 software (WaveMetrics).

Molecular Biology, Protein Expression, and Protein Purification. Na_VAb/FY was constructed by site-directed mutagenesis (QuikChange; Agilent) and confirmed by sequencing. Na_VAb/1–226 was constructed by the introduction of a stop codon in place of Lys-227 and confirmed by sequencing. Recombinant baculovirus was generated by using the Bac-to-Bac system (Invitrogen), and then *Trichopulsia ni* cells were infected for protein production. Protein was produced and purified as described (8).

Na_VAb Crystallization and Data Collection. Na_VAb/FY and Na_VAb/1–226 were reconstituted into 1,2-dimyristoyl-*sn*-glycero-3-phosphatidylcholine (DMPC): CHAPSO bicelles (Anatrace) as described (7), and then mixed in a 1:2 ratio and set up in a hanging-drop format over well solutions containing 1.8 M ammonium sulfate and 100 mM sodium acetate (pH 4.8). Crystals appeared in 3–5 d and grew to full size within 1 wk (∼50 by 100 μm). They were cryoprotected by slow addition of well solution supplemented with increasing concentration of glucose. Final glucose concentration was 30% after this procedure, and then crystals were harvested in nylon loops and plunged into liquid nitrogen for data collection.

Data were collected at Advanced Light Source (beamlines BL821 and BL822), with diffraction quality and resolution substantially improved from previous reports. Most Na_VAb crystals diffracted to better than 4 Å—the data reported herein were collected from single crystals, collected at 0.9999–1.1000 Å. As reported previously, crystals were highly radiation sensitive, and exposure times were minimized to limit decay during data collection.

Structure Determination and Refinement. X-ray diffraction data were integrated and scaled with DENZO/SCALEPACK (51), and then processed with PHENIX (52). The Na_VAb/FY structure was solved with molecular replacement by using the voltage sensor and selectivity filter of Na_VAb [Protein Data Bank (PDB) ID code 3RVY] as search model. The Na_VAb/1–226 structure was solved with molecular replacement, by using the voltage sensor of Na_VAb/I217C as a starting model. After initial phases, models of both proteins were manually rebuilt based on resulting electron-density maps. Tight NCS restraints were applied throughout the early stages of refinement of Na_VAb/FY and clearly improved our electron-density maps. Electron density was easily interpretable throughout the CTD for all four chains of Na_VAb/FY, although side chains could not be visualized near the C terminus. As noted in the text, electron density was weak for the C-terminal portion of S6 of Na_VAb/1–226 and could not be modeled for any amino acids past D219. Simulated annealing omit maps were used to confirm the placement of the S6 at the activation gate, as well as the position of the S4–S5 linker. Lipids and waters were added to both models near the end of refinement, and then NCS restraints were relaxed in the final stages. Geometry, B factors, and electron-density fits were assessed with POLYGON (53).

Molecular Dynamics. All-atom molecular models of the Na_VAb I217C mutant (PDB ID code: 3RVY) (8) and NavAb/1–226 were constructed by embedding each structure in a hydrated DMPC bilayer, with ∼250 mM NaCl and ∼170 mM NaCl, respectively. The NavAb/1–226 model was modified with the V213A/I217A mutation after membrane embedding to obtain the NavAb/AA system. The protein, lipids, and ions were modeled with the CHARMM36 all-atom force field (54–56), and water molecules were modeled with TIP3P (57). All unbiased simulations were performed with GROMACS (Version 4.6.5) (58) at constant temperature (300 K) and pressure (1 atm). Restrained models of Na_VAb/1–226 and Na_VAb/AA, were prepared by imposing harmonic potentials with force constants of 1 $kcal\cdot mol^{-1}\cdot Å^{-2}$ on all Cα atoms of transmembrane helices S5 and S6, restraining them near the crystallographic state. Fifteen simulation repeats were generated for the Na_VAb/I217C system (1,000 ns each), and 10 simulation repeats were generated for each of the four open-state systems (600 ns each), with aggregate simulation time of 39 μs. All replicas of all systems began with 30 ns of protein-restrained equilibration not included in analysis.

For the four open-state systems, snapshots were extracted from five independent simulation repeats at $t = 100$ ns and were subsequently used as initial conditions for umbrella sampling (US) simulations. We used biased sampling to study the movement of Na^+ along the channel axis from within the CC to bulk water on the intracellular side of the membrane. Production simulations were performed for ∼55 ns per umbrella with a harmonic restraining potential force constant of 2.39 $kcal\cdot mol^{-1}\cdot Å^{-2}$ and a flat-bottom cylindrical position restraint on the target Na^+. All US simulations were performed with GROMACS (Version 5.0.6) (59). The axial position of the permeating Na^+ was used to generate five independent potential of mean force (PMF) profiles, for each of the open systems. We report the average PMF for Na^+ movement along the channel axis with error bars computed by using the SE of mean over all five PMFs. The aggregate simulation time of the US simulations was ∼39 μs (715 windows in total, multiplied by 55 ns).

For additional details of system set up and equilibration, simulation protocol, and analysis, see *SI Methods*.

1. Hille B (2001) *Ionic Channels of Excitable Membranes* (Sinauer, Sunderland, MA), 3rd Ed.
2. George AL, Jr (2005) Inherited disorders of voltage-gated sodium channels. *J Clin Invest* 115(8):1990–1999.
3. Catterall WA (2000) From ionic currents to molecular mechanisms: the structure and function of voltage-gated sodium channels. *Neuron* 26(1):13–25.
4. Ren D, et al. (2001) A prokaryotic voltage-gated sodium channel. *Science* 294(5550): 2372–2375.
5. Catterall WA, Zheng N (2015) Deciphering voltage-gated Na$^+$ and Ca^{2+} channels by studying prokaryotic ancestors. *Trends Biochem Sci* 40(9):526–534.
6. Payandeh J, Minor DL, Jr (2015) Bacterial voltage-gated sodium channels (BacNa$_V$s) from the soil, sea, and salt lakes enlighten molecular mechanisms of electrical signaling and pharmacology in the brain and heart. *J Mol Biol* 427(1):3–30.
7. Payandeh J, Scheuer T, Zheng N, Catterall WA (2011) The crystal structure of a voltage-gated sodium channel. *Nature* 475(7356):353–358.
8. Payandeh J, Gamal El-Din TM, Scheuer T, Zheng N, Catterall WA (2012) Crystal structure of a voltage-gated sodium channel in two potentially inactivated states. *Nature* 486(7401):135–139.
9. Zhang X, et al. (2012) Crystal structure of an orthologue of the NaChBac voltage-gated sodium channel. *Nature* 486(7401):130–134.
10. McCusker EC, et al. (2012) Structure of a bacterial voltage-gated sodium channel pore reveals mechanisms of opening and closing. *Nat Commun* 3:1102.
11. Shaya D, et al. (2014) Structure of a prokaryotic sodium channel pore reveals essential gating elements and an outer ion binding site common to eukaryotic channels. *J Mol Biol* 426(2):467–483.
12. Bezanilla F (2000) The voltage sensor in voltage-dependent ion channels. *Physiol Rev* 80(2):555–592.
13. Catterall WA (2010) Ion channel voltage sensors: Structure, function, and pathophysiology. *Neuron* 67(6):915–928.
14. DeCaen PG, Yarov-Yarovoy V, Zhao Y, Scheuer T, Catterall WA (2008) Disulfide locking a sodium channel voltage sensor reveals ion pair formation during activation. *Proc Natl Acad Sci USA* 105(39):15142–15147.
15. DeCaen PG, Yarov-Yarovoy V, Sharp EM, Scheuer T, Catterall WA (2009) Sequential formation of ion pairs during activation of a sodium channel voltage sensor. *Proc Natl Acad Sci USA* 106(52):22498–22503.
16. DeCaen PG, Yarov-Yarovoy V, Scheuer T, Catterall WA (2011) Gating charge interactions with the S1 segment during activation of a Na$^+$ channel voltage sensor. *Proc Natl Acad Sci USA* 108(46):18825–18830.
17. Gamal El-Din TM, Scheuer T, Catterall WA (2014) Tracking S4 movement by gating pore currents in the bacterial sodium channel NaChBac. *J Gen Physiol* 144(2):147–157.
18. Bagnéris C, Naylor CE, McCusker EC, Wallace BA (2015) Structural model of the open-closed-inactivated cycle of prokaryotic voltage-gated sodium channels. *J Gen Physiol* 145(1):5–16.
19. Ragsdale DS, McPhee JC, Scheuer T, Catterall WA (1994) Molecular determinants of state-dependent block of Na$^+$ channels by local anesthetics. *Science* 265(5179):1724–1728.
20. Ragsdale DS, McPhee JC, Scheuer T, Catterall WA (1996) Common molecular determinants of local anesthetic, antiarrhythmic, and anticonvulsant block of voltage-gated Na$^+$ channels. *Proc Natl Acad Sci USA* 93(17):9270–9275.
21. Gamal El-Din TM, Martinez GQ, Payandeh J, Scheuer T, Catterall WA (2013) A gating charge interaction required for late slow inactivation of the bacterial sodium channel NavAb. *J Gen Physiol* 142(3):181–190.
22. Armstrong CM, Bezanilla F, Rojas E (1973) Destruction of sodium conductance inactivation in squid axons perfused with pronase. *J Gen Physiol* 62(4):375–391.
23. Arrigoni C, et al. (2016) Unfolding of a temperature-sensitive domain controls voltage-gated channel activation. *Cell* 164(5):922–936.
24. Irie K, Shimomura T, Fujiyoshi Y (2012) The C-terminal helical bundle of the tetrameric prokaryotic sodium channel accelerates the inactivation rate. *Nat Commun* 3:793.
25. Jiang Y, et al. (2002) The open pore conformation of potassium channels. *Nature* 417(6888):523–526.
26. Zhao Y, Scheuer T, Catterall WA (2004) Reversed voltage-dependent gating of a bacterial sodium channel with proline substitutions in the S6 transmembrane segment. *Proc Natl Acad Sci USA* 101(51):17873–17878.
27. Zhao Y, Yarov-Yarovoy V, Scheuer T, Catterall WA (2004) A gating hinge in Na$^+$ channels; a molecular switch for electrical signaling. *Neuron* 41(6):859–865.
28. Cuello LG, et al. (2010) Structural basis for the coupling between activation and inactivation gates in K$^+$ channels. *Nature* 466(7303):272–275.
29. Hille B (1977) Local anesthetics: Hydrophilic and hydrophobic pathways for the drug-receptor reaction. *J Gen Physiol* 69(4):497–515.
30. Courtney KR (1975) Mechanism of frequency-dependent inhibition of sodium currents in frog myelinated nerve by the lidocaine derivative GEA. *J Pharmacol Exp Ther* 195(2):225–236.
31. Chakrabarti N, et al. (2013) Catalysis of Na$^+$ permeation in the bacterial sodium channel Na$_V$Ab. *Proc Natl Acad Sci USA* 110(28):11331–11336.
32. Lenaeus M, et al. (2017) Open and closed states of the Na$_V$Ab activation gate. *Biophys J* 112(3):104a.
33. Jensen MØ, et al. (2012) Mechanism of voltage gating in potassium channels. *Science* 336(6078):229–233.
34. Bagnéris C, et al. (2013) Role of the C-terminal domain in the structure and function of tetrameric sodium channels. *Nat Commun* 4:2465.
35. Kintzer AF, Stroud RM (2016) Structure, inhibition and regulation of two-pore channel TPC1 from *Arabidopsis thaliana*. *Nature* 531(7593):258–262.
36. Guo J, et al. (2016) Structure of the voltage-gated two-pore channel TPC1 from *Arabidopsis thaliana*. *Nature* 531(7593):196–201.
37. Boiteux C, Vorobyov I, Allen TW (2014) Ion conduction and conformational flexibility of a bacterial voltage-gated sodium channel. *Proc Natl Acad Sci USA* 111(9):3454–3459.
38. Wilman HR, Shi J, Deane CM (2014) Helix kinks are equally prevalent in soluble and membrane proteins. *Proteins* 82(9):1960–1970.
39. Zhou Y, Morais-Cabral JH, Kaufman A, MacKinnon R (2001) Chemistry of ion coordination and hydration revealed by a K$^+$ channel-Fab complex at 2.0 A resolution. *Nature* 414(6859):43–48.
40. Jensen MO, et al. (2010) Principles of conduction and hydrophobic gating in K$^+$ channels. *Proc Natl Acad Sci USA* 107(13):5833–5838.
41. Aryal P, Sansom MS, Tucker SJ (2015) Hydrophobic gating in ion channels. *J Mol Biol* 427(1):121–130.
42. Zhu F, Hummer G (2012) Drying transition in the hydrophobic gate of the GLIC channel blocks ion conduction. *Biophys J* 103(2):219–227.
43. Neale C, Chakrabarti N, Pomorski P, Pai EF, Pomès R (2015) Hydrophobic gating of ion permeation in magnesium channel CorA. *PLOS Comput Biol* 11(7):e1004303.
44. Shafrir Y, Durell SR, Guy HR (2008) Models of the structure and gating mechanisms of the pore domain of the NaChBac ion channel. *Biophys J* 95(8):3650–3662.
45. Oelstrom K, Goldschen-Ohm MP, Holmgren M, Chanda B (2014) Evolutionarily conserved intracellular gate of voltage-dependent sodium channels. *Nat Commun* 5:3420.
46. Oelstrom K, Chanda B (2016) Congruent pattern of accessibility identifies minimal pore gate in a non-symmetric voltage-gated sodium channel. *Nat Commun* 7:11608.
47. Arcisio-Miranda M, Muroi Y, Chowdhury S, Chanda B (2010) Molecular mechanism of allosteric modification of voltage-dependent sodium channels by local anesthetics. *J Gen Physiol* 136(5):541–554.
48. Muroi Y, Arcisio-Miranda M, Chowdhury S, Chanda B (2010) Molecular determinants of coupling between the domain III voltage sensor and pore of a sodium channel. *Nat Struct Mol Biol* 17(2):230–237.
49. Chanda B, Bezanilla F (2002) Tracking voltage-dependent conformational changes in skeletal muscle sodium channel during activation. *J Gen Physiol* 120(5):629–645.
50. Capes DL, Goldschen-Ohm MP, Arcisio-Miranda M, Bezanilla F, Chanda B (2013) Domain IV voltage-sensor movement is both sufficient and rate limiting for fast inactivation in sodium channels. *J Gen Physiol* 142(2):101–112.
51. Otwinowski Z, Minor W (1997) Processing of X-ray diffraction data collected in oscillation mode. *Methods Enzymol* 276:307–326.
52. Adams PD, et al. (2010) PHENIX: A comprehensive Python-based system for macromolecular structure solution. *Acta Crystallogr D Biol Crystallogr* 66(Pt 2):213–221.
53. Urzhumtseva L, Afonine PV, Adams PD, Urzhumtsev A (2009) Crystallographic model quality at a glance. *Acta Crystallogr D Biol Crystallogr* 65(Pt 3):297–300.
54. Best RB, et al. (2012) Optimization of the additive CHARMM all-atom protein force field targeting improved sampling of the backbone φ, ψ and side-chain $\chi(1)$ and $\chi(2)$ dihedral angles. *J Chem Theory Comput* 8(9):3257–3273.
55. MacKerell AD, et al. (1998) All-atom empirical potential for molecular modeling and dynamics studies of proteins. *J Phys Chem B* 102(18):3586–3616.
56. Klauda JB, et al. (2010) Update of the CHARMM all-atom additive force field for lipids: Validation on six lipid types. *J Phys Chem B* 114(23):7830–7843.
57. Jorgensen W, Chandrasekhar J, Madura JD, Impey RW, Klein M (1983) Comparison of simple potential functions for simulating water. *J Chem Phys* 79(2):926–935.
58. Hess B, Kutzner C, van der Spoel D, Lindahl E (2008) GROMACS 4: Algorithms for highly efficient, load-balanced, and scalable molecular simulation. *J Chem Theory Comput* 4(3):435–447.
59. Abraham MJ, et al. (2015) GROMACS: High performance molecular simulations through multi-level parallelism from laptops to supercomputers. *SoftwareX* 1-2:19–25.
60. Jefferys E, Sands ZA, Shi J, Sansom MS, Fowler PW (2015) Alchembed: A computational method for incorporating multiple proteins into complex lipid geometries. *J Chem Theory Comput* 11(6):2743–2754.
61. Wu EL, et al. (2014) CHARMM-GUI Membrane Builder toward realistic biological membrane simulations. *J Comput Chem* 35(27):1997–2004.
62. Fiser A, Sali A (2003) Modeller: Generation and refinement of homology-based protein structure models. *Methods Enzymol* 374:461–491.
63. Noskov SY, Roux B (2008) Control of ion selectivity in LeuT: Two Na$^+$ binding sites with two different mechanisms. *J Mol Biol* 377(3):804–818.
64. Venable RM, Luo Y, Gawrisch K, Roux B, Pastor RW (2013) Simulations of anionic lipid membranes: Development of interaction-specific ion parameters and validation using NMR data. *J Phys Chem B* 117(35):10183–10192.
65. Darden T, York D, Pedersen L (1993) Particle mesh Ewald: An N -log(N) method for Ewald sums in large systems. *J Chem Phys* 98(12):10089–10092.
66. Essmann U, et al. (1995) A smooth particle mesh Ewald method. *J Chem Phys* 103(19): 8577–8593.
67. Verlet L (1967) Computer “experiments” on classical fluids. I. Thermodynamical properties of Lennard-Jones molecules. *Phys Rev* 159(1):98–103.
68. Hoover WG (1985) Canonical dynamics: Equilibrium phase-space distributions. *Phys Rev A Gen Phys* 31(3):1695–1697.
69. Nosé S (1984) A molecular dynamics method for simulations in the canonical ensemble. *Mol Phys* 52(2):255–268.
70. Parrinello M, Rahman A (1980) Crystal structure and pair potentials: A molecular-dynamics study. *Phys Rev Lett* 45(14):1196–1199.
71. Nosé S, Klein ML (1983) Constant pressure molecular dynamics for molecular systems. *Mol Phys* 50(5):1055–1076.
72. Hess B (2008) P-LINCS: A parallel linear constraint solver for molecular simulation. *J Chem Theory Comput* 4(1):116–122.
73. Hub JS, de Groot BL, van der Spoel D (2010) g_wham—a free weighted histogram analysis implementation including robust error and autocorrelation estimates. *J Chem Theory Comput* 6(12):3713–3720.